Available online at www.sciencedirect.com
ScienceDirect
Trans. Nonferrous Met. Soc. China 34(2024) 423−434
Transactions of Nonferrous Metals Society of China
www.tnmsc.cn

Effect of deposition strategies on microstructures, defects and mechanical properties of 5356 aluminum alloy by wire arc additive manufacturing

Kai ZHU, Jian WANG, Wei-chen ZHANG, Xiao-lei ZHU, Xiao-feng LU

School of Mechanical and Power Engineering, Nanjing Tech University, Nanjing 211816, China

Received 19 July 2022; accepted 6 March 2023

Abstract: Wire arc additive manufacturing (WAAM) is performed to study the effects of three deposition strategies on the 5356 aluminum alloy (AA5356) components. Three deposition strategies are reciprocating scanning (RS), oscillating scanning (OS) and vertical scanning (VS), respectively. The microstructures, defects and mechanical properties of AA5356 components are fundamentally explored. The results show that the VS strategy makes the uniform heat distribution of components. The microstructures with the VS strategy are mainly composed of equiaxed grains, compared with those with RS and OS strategies. The equiaxed grains lead to the highest microhardness (HV 77.25). The porosity and micropore size of the component with the VS strategy are reduced by 45.52% and 19.81%, respectively, resulting in improved tensile properties. Thus, the VS strategy provides a new solution for obtaining AA5356 components with uniform microstructure and excellent mechanical properties.

Key words: wire arc additive manufacturing; deposition strategy; aluminum alloys; microstructure; mechanical properties

1 Introduction

In recent years, wire arc additive manufacturing (WAAM) is becoming a new promising economical technique for metal additive manufacturing. WAAM has fast deposition speed, simple equipment, and high material utilization [1,2], suitable for the processing and manufacturing medium and large structural components such as cruciform, stiffened panels, and wing ribs [3]. Cold metal transfer (CMT) welding is an enhanced gas metal arc welding (GMAW) characterized by a highly stable arc with a minor splash, low heat input, and high deposition rate [4]. CMT arc modes consist of pulse, advanced, and pulse advanced variants. These variants are suitable for WAAM processes, which produce different droplet transfers and heat inputs [5].

Several researchers have investigated the application of WAAM on various materials like Al alloy [6], Ti alloy [7], nickel-based alloy [8], and steel [9]. WAAM-CMT Al alloy is mainly studied from two aspects: one is controlling deposition accuracy, and the other is controlling the properties of deposited components. Many researchers studied the effects of deposition parameters on the deposition accuracy, porosity, and mechanical properties of WAAM components, such as droplet transfer mode, current, voltage, wire feeding speed, travelling speed, heat input, interpass temperature, etc [10−15]. To improve the surface quality of the WAAM Al alloy components, JAFARI et al [16] studied the influence of travelling speed and wire feeding speed on the deposition accuracy of single-pass cladding and single-pass multilayer cladding rings. The researchers found that increasing the travelling speed improves the width accuracy by decreasing the heat input. During the deposition process, OYAMA et al [17] monitored

Corresponding author: Jian WANG, Tel: +86-25-58139352, E-mail: njjwang@njtech.edu.cn;
Xiao-feng LU, Tel: +86-25-58139356, E-mail: xflu@njtech.edu.cn
DOI: 10.1016/S1003-6326(23)66408-8

the size and geometry of the molten pool in real time. They found that changing the heat input effectively enhances the deposition efficiency and the dimensional accuracy of the deposited component. Due to the heat source staying longer at the edge, the high heat input in thin-walled structures makes it difficult to achieve highly accurate dimensional accuracy in continuous deposition with staggered deposition. At the same time, some researchers studied the control of the properties of WAAM Al alloy. Many researchers studied the mechanical properties of as-deposited 2xxx, 4xxx, 5xxx, and 6xxx series of WAAM Al alloys. GU et al [18] reported that the ultimate tensile strength (UTS) and yield strength (YS) of WAAM-CMT AA2219 are 260 and 126 MPa, respectively. Accordingly, they improved the UTS and YS of WAAM AA2219 to 450 and 305 MPa, respectively, by T6 heat treatment process and interlayer rolling method. MIAO et al [19] demonstrated that the UTS and YS of the WAAM AA4043 are 152 and 70 MPa, respectively, and were enhanced by laser-arc-hybrid additive manufacturing process to 164 and 76 MPa, respectively. SU et al [12] reported that the UTS and YS of the WAAM AA5356 are 255 and 128 MPa, respectively, and WAAM-CMT AA5356 components have a better mechanical performance compared to 5356 casting alloys. KLEIN et al [20] applied the T6 heat treatment process to improve the UTS and YS of WAAM AA6063 from 161 and 81 MPa to 287 and 266 MPa, respectively. However, plasticity decreases by about 70% in the meantime.

There are various studies concerning the parameters adjustment for the mechanical properties of WAAM components improvement; however, few studies focus on the deposition strategies. CABALLERO et al [21] conducted experiments to determine the effects of varying process parameters on microstructures and mechanical properties of 17-4 PH stainless steel components, including different deposition strategies (single, oscillating, and parallel scanning). SYED et al [22] investigated the effects of two different deposition strategies, oscillating and parallel strategies, on the tensile and the high-cycle fatigue properties of WAAM Ti−6Al−4V alloys. The results showed that the oscillating strategy samples have lower fatigue strength than parallel pass strategy samples. On the one hand, XU et al [23] compared the effects of parallel channels, triangular oscillating, and square oscillating on the bead geometry. The results showed that the triangular oscillating strategy is the most recommended for martensitic aging steels. On the other hand, MA et al [24] comprehensively studied oscillating strategies for depositing large and thin-walled aluminum alloy structures. The aim is using the oscillating strategy to improve surface flatness.

In summary, the deposition strategy affects the forming quality and mechanical properties of WAAM components. This study presents a new vertical scanning deposition strategy based on the oscillating scanning. Microstructure observations, micropore analysis and mechanical properties tests are adapted to reveal the influence of deposition strategy. The deposition strategy acting as an important parameter will be helpful to manufacture WAAM large aluminum alloy components.

2 Experimental

The WAAM system mainly comprised a Fronius CMT welding machine, a wire feeder, and a three-axis CNC machine. The ER5356 alloy filler wire with 1.2 mm in diameter and 6061-T6 aluminum alloy plate as substrate with 200 mm × 200 mm × 15 mm were used. Table 1 listed the elemental compositions of the wire and substrate. Before processing, all substrates were cleaned with acetone and a steel brush, and the filler wire was maintained dry. The experimental parameters were as follows: The travelling speed was 600 mm/min, the wire feeding speed was 7.3 m/min, the contact tip-to-work distance was kept at 10 mm, the waiting time was 60 s, the *Z*-increment value was set to be 3 mm, and 99.999% argon with 25 L/min flow rate was employed. The samples deposited 10 layers respectively using three deposition strategies, each layer being a square with a side length of 160 mm. The first four layers were preheating layers, and the fifth to tenth layers were used to obtain microstructure and microhardness of the samples. Figure 1 showed WAAM AA5356 components. Figure 1(b) showed the WAAM components using three deposition strategies. Reciprocating scanning (RS) meant that the deposition direction between adjacent welds was the same, parallel to the *Y*-axis direction, while the deposition direction of the adjacent deposition layer was opposite. Oscillating

Table 1 Chemical compositions of ER5356 welding wire and AA6061 substrate (wt.%)

Material	Mg	Zn	Cu	Si	Fe	Mn	Cr	Ti	Al
AA6061	1.13	0.004	0.23	0.593	0.29	0.05	0.19	0.031	Bal.
ER5356	4.80	0.010	0.01	0.040	0.11	0.14	0.10	0.085	Bal.

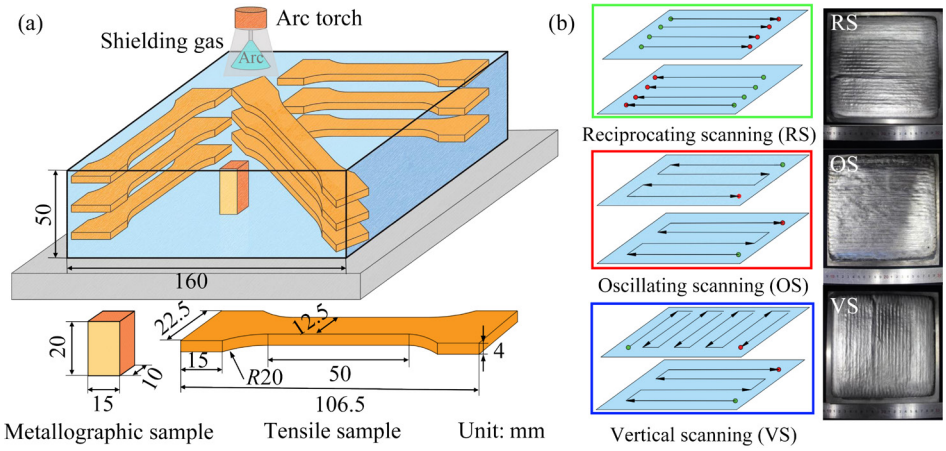

Fig. 1 WAAM AA5356 components: (a) Sampling position and sizes of metallographic and tensile samples; (b) Deposition strategies and physical drawings of WAAM AA5356 components

scanning (OS) strategy referred to the continuous deposition of each sedimentary layer without arc extinguishing, and the arc starting point of adjacent sedimentary layers was opposite to the arc extinguishing point. Vertical scanning (VS) strategy meant that each sedimentary layer was deposited through oscillatory scan. The scanning paths of adjacent sedimentary layers were perpendicular to each other (the red dot represents the arc starting point, and the green dot represents the arc extinguishing point).

Figure 1(a) showed the WAAM process, sampling position, and size of metallography and tensile samples. Tensile samples were taken from three directions: parallel to the *X*-axis (marked as *X*), parallel to the *Y*-axis (marked as *Y*), and the 45° between the *XY* axis (marked as 45°), and tensile samples of each direction were taken from the bottom (the 1st layer and the 2nd layer), the middle (the 3rd layer and the 4th layer) and the top (the 5th layer and the 6th layer). Optical microscope (OM) samples were mechanically ground to 2000 grit SiC paper and polished with 1 μm adamantine plaster. Samples were etched at 20 V in a 2.5 wt.% HBF_4 solution for 60 s to investigate the microstructure. The microstructures were observed via OM (Keyence VHX−6000) under polarized light. The grain sizes were measured by Image J software. The dimensions of each grain were depicted along the grain boundary, and the areas of each grain were calculated. Macroscopic metallography was taken along the *ZOY* plane in WAAM AA5356 components to analyze the microhardness. A scanning electron microscope (SEM, FEI Quanta650) was equipped with energy disperse spectroscopy (EDS, OXFORD Ultim Extreme) to reveal delicate structures. The micropores within the WAAM samples were examined using X-ray diffraction topography (XRT) equipment (Xradia V ERSA XRM−500 system). Cube samples with a volume of 1 mm^3 were respectively taken from the bottom to top of XRT samples. XRT was used to perform a series of image processing analyses with the open source P3 and P3B software. The 16-bit images were converted to 8-bit with a grayscale value ranging from 0 to 255. After cropping into the appropriate size of each image, the visualization tool software Avizo was introduced to reconstruct 3D distribution images of micropores and microstructures. To suppress errors originating from image noise, micropores containing >238 voxels or equivalent diameters of >5 μm were counted for quantitative analysis. The micro-hardness was measured by a Zwick Roell indented ZHV2 system using a 0.3 mm distance between indentations. The tensile tests were performed using an Instron 3367 electronic universal material testing machine with a 30 kN load cell at a 1 mm/min deformation rate and room temperature.

3 Results and discussion

3.1 Macrostructure and microstructure

Figure 2 shows the macroscopic metallography of WAAM AA5356 components with three deposition strategies. The remelting interface is easy to identify. The height of each layer under the three deposition strategies is roughly the same. As shown in Figs. 2(a−c), the samples of the three deposition strategies have a certain number of micropore defects. Besides, most micropores are located in the interlayer area. Micropores generally exist in three forms: regular round, irregular void, and chain-like, mainly due to the deposition of hydrogen and impurities in the welding wire [25,26].

Figure 3 shows microstructure characteristics of WAAM components with three deposition strategies, respectively. The micro-structures of WAAM AA5356 components with three deposition strategies are mainly equiaxed grains, with a small number of columnar grains distributed. These columnar grains grow in the temperature gradient direction because grain growth is usually in the same direction as heat dissipation, as shown in Fig. 3(h). The microstructures of the bottom region mainly consist of equiaxed grains, and the size of equiaxed grains is small. The microstructures of the middle region are still dominated by equiaxed grains. The number of columnar grains increases, and the size of equiaxed grains increases. The microstructures of the top region are significantly different from those of the bottom region.

Figure 4 shows the grain sizes of WAAM AA5356 components with each deposition strategy in bottom, middle, and top regions. The grain diameter of WAAM AA5356 components increases with increasing the deposition height. The average grain size of components with RS strategy increases from 79.17 to 96.75 μm, and the growth rate is 22.20%. The average grain size of components with OS strategy increases from 84.84 to 117.86 μm, and the growth rate is 38.92%. The average grain size of aluminum alloy components with VS strategy increases from 86.60 to 104.74 μm, and the growth rate is 20.94%. The grain size in the bottom region is mainly concentrated within 70−90 μm. With

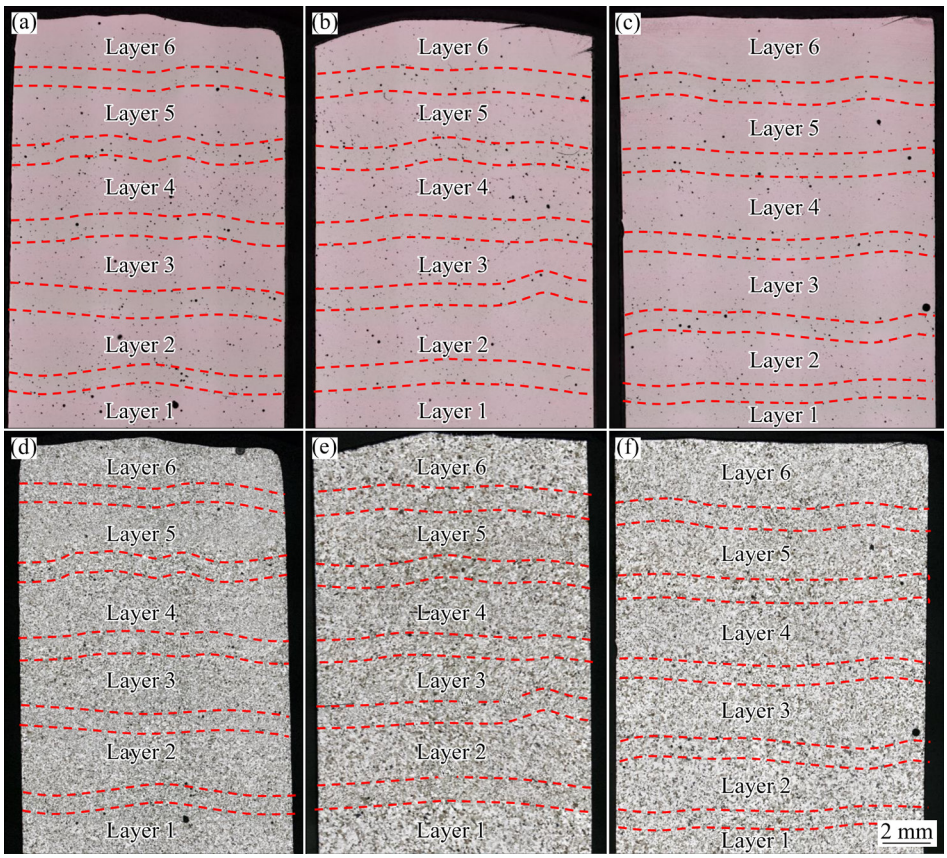

Fig. 2 Macroscopic metallographs of WAAM AA5356 components: (a−c) Polish state for RS, OS and VS strategies, respectively; (d−f) Corrosion state for RS, OS and VS strategies, respectively

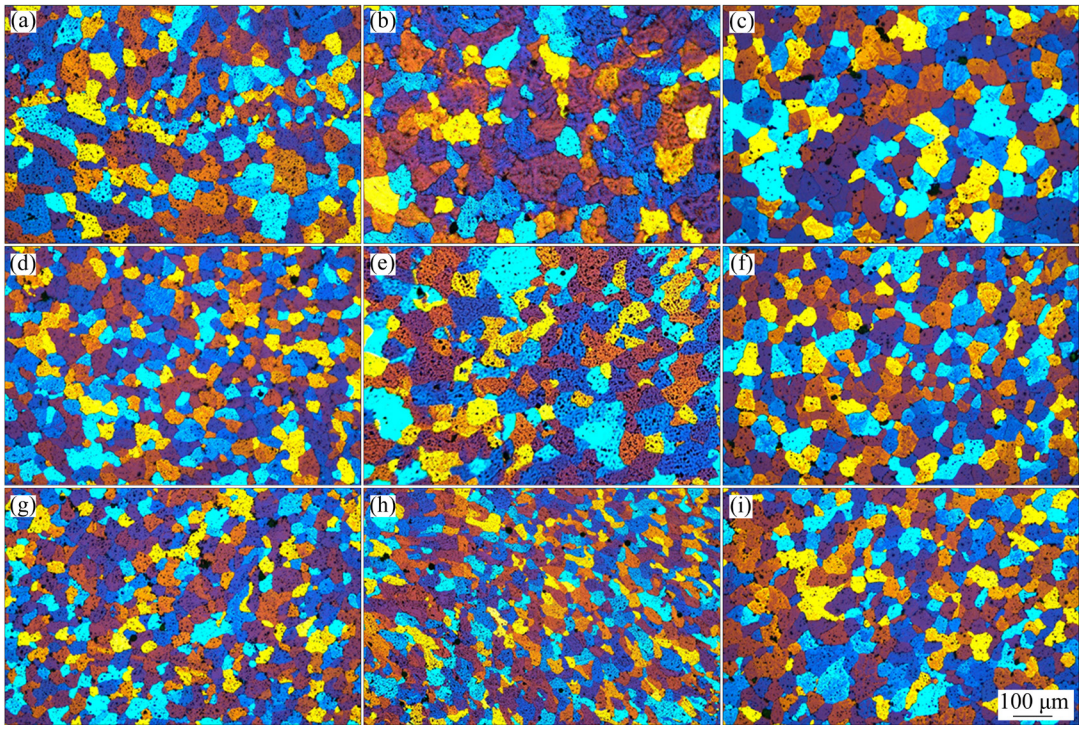

Fig. 3 Microstructures of WAAM AA5356 components: (a−c) Top grain with RS, OS and VS strategies, respectively; (d−f) Middle grain with RS, OS and VS strategies, respectively; (g−i) Bottom grain with RS, OS and VS strategies, respectively

increasing the deposition height, large size grains (170−200 μm) appear, and the proportion gradually increases, increasing the overall average grain size, especially the process from the bottom grain to the middle grain of WAAM AA5356 component with OS strategy, as shown in Figs. 4(e, h). To better represent the change in grain size, the Gaussian function is used to fit the histogram into a curve, and the formula is as follows:

$$G_{\mathrm{d}} = A\exp[(G_{\mathrm{s}} - B)^2/(-2C^2)] \quad (1)$$

where grain distribution is defined as the G_{d}, grain size is defined as the G_{s}, and A, B, and C are the coefficients of the Gaussian function. The value of A is the most extensive grain distribution, B is the grain size of the largest grain distribution, and C is the uniformity of grain size distribution.

The heat accumulation effect of the additive manufacturing process is the main reason for the microstructure transformation. In the early stage of WAAM, strong heat absorption and dissipation occurred on the substrate surface under the action of high-temperature arc, resulting in large undercooling [27]. The substrate has more grain nucleus. The grain nucleus competes when growing in all directions. With the increase of deposition height, the heat accumulation effect of WAAM gradually enhances the preheating effect of the lower layer on the upper layer. The heat accumulation indirectly increases the heat input of upper layer and improves the overall temperature of the molten pool. Due to the high-temperature existence time of liquid metal and the slow cooling rate, the grain sizes become large [28].

Compared with the RS strategy, the average grain sizes of components with OS and VS strategies are larger. Due to RS strategy continuous arc initiation and extinction in the WAAM process, the overall composition has low heat input and low-temperature gradient, resulting in small grain size. There is no arc extinction in the WAAM process with OS and VS strategies, resulting in too high heat input, large temperature gradient, and large grain size. Because the deposition paths under OS strategy are identical, the heat accumulation of VS strategy is more dispersed than that of OS strategy, and the grain growth has no obvious direction.

In addition, the electromagnetic force of CMT-advanced mode is larger than that of other

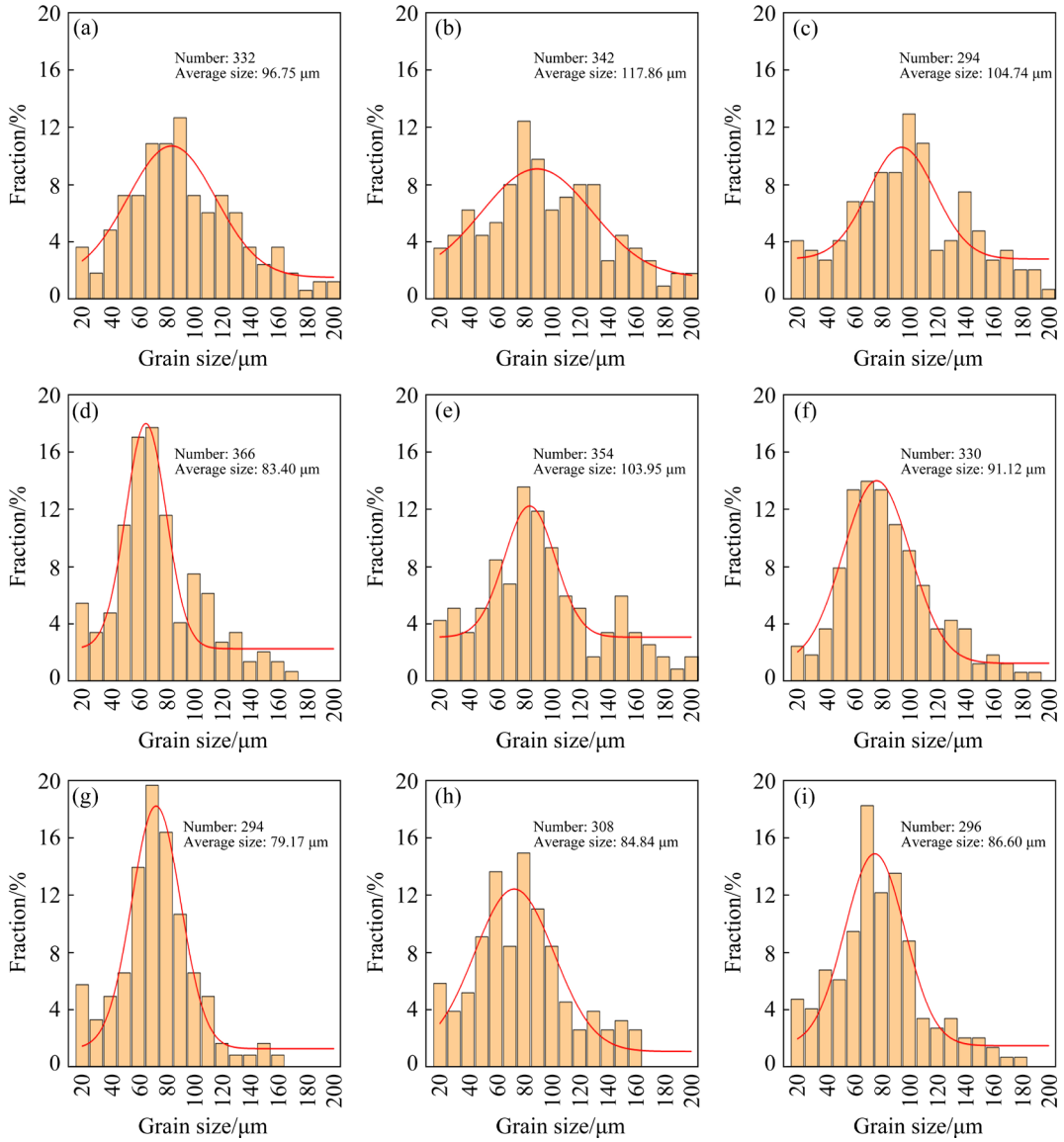

Fig. 4 Grain size distributions of WAAM AA5356 components: (a−c) Top grain with RS, OS and VS strategies, respectively; (d−f) Middle grain with RS, OS and VS strategies, respectively; (g−i) Bottom grain with RS, OS and VS strategies, respectively

mode which means stronger stirring effect on the melt pool, resulting in smaller grain size [29]. Since the electric arc creates electromagnetic force and plasma flow force, those forces prompt melt flow in melt pool and change with arc current and its waveform [29,30]. According to the principle of electromagnetic induction, the directions of the forces change with the electrode polarity or the direction of the arc current. The solidification process of melt pool which produces the microstructure depends on these forces. The growing columnar dendrites based on the previous grain lattice are impacted by the strong oscillation stirring from the dramatically changed forces. Consequently, the columnar dendrites cannot continue to grow. The impacted dendrites are partially molten [31]. Therefore, the microstructure of the samples in the CMT-advanced mode is the uniform equiaxed grain.

3.2 Micropores

Aluminum alloy is one of the alloys more prone to porosity during WAAM. Porosity is one of the internal defects that usually adversely affect the fatigue, strength, and toughness of aluminum alloy [32]. Hydrogen in the aluminum alloy is considered the main factor for forming micropores in the WAAM process. As the temperature

decreases, the hydrogen solubility of liquid aluminum decreases rapidly, almost 20 times higher than that of solid aluminum [33]. Because the insoluble hydrogen in aluminum is discharged from the solid−liquid interface to the surrounding liquid, the hydrogen is supersaturated, and finally micropores are formed in the solidified metal.

XRT experiments on components with RS, OS and VS strategies were carried out. Due to the resolution, the micropores with an equivalent diameter of less than 4 μm are not marked. Figure 5 shows the experimental results. The equivalent diameter of the micropores is mainly concentrated at 5−20 μm. Figure 5(a) show that there exist rare micropores with a size larger than 100 μm in all samples. As shown in Fig. 5(b), the average diameter of the micropore with the RS strategy is the largest (8.53 μm). The average diameter of the micropore with VS strategy is the smallest (6.84 μm) This is mainly due to a certain number of micropores with VS strategy whose diameter is less than 5 μm. As shown in Figs. 5(c−e), the porosity with RS, OS and VS strategies is 0.883%, 0.703%, and 0.481%, respectively. This is because the RS strategy is an intermittent arc initiation and extinguishing process, which results in a large gap between adjacent molten pools and easy to produce micropores. In addition, due to the large heat input with OS and VS strategies, the liquid molten pool is exposed to the air for a longer time, and most of the hydrogen will escape before solidification.

Coarsening and Ostwald ripening, which may increase the size and roundness of micropores, are inevitable for micropores in aluminum alloys during high-temperature exposure. However, due to their different evolution behaviors, coarsening and Ostwald ripening are not predominant for the evolution of micropores in the various sections of WAAM Al alloys. Figure 6 shows three typical shapes of micropores. The formation of micropores during deposition involves three main mechanisms based on the typical shapes. Firstly, micropores with near-spherical shapes are formed by entrapped hydrogen [25], as shown in Fig. 6(a). The mechanism is the formation of hydrogen micropores during the solidification process. The supersaturated hydrogen atoms precipitate as molecules, and the shape of the micropores becomes increasingly rounded during the deposition process due to the internal pressure of the micropores against the surface tension. Secondly, micropores with rough surface morphology are formed by the wire's impurities [26], as shown in Fig. 6(b). The particles and dendrites provide

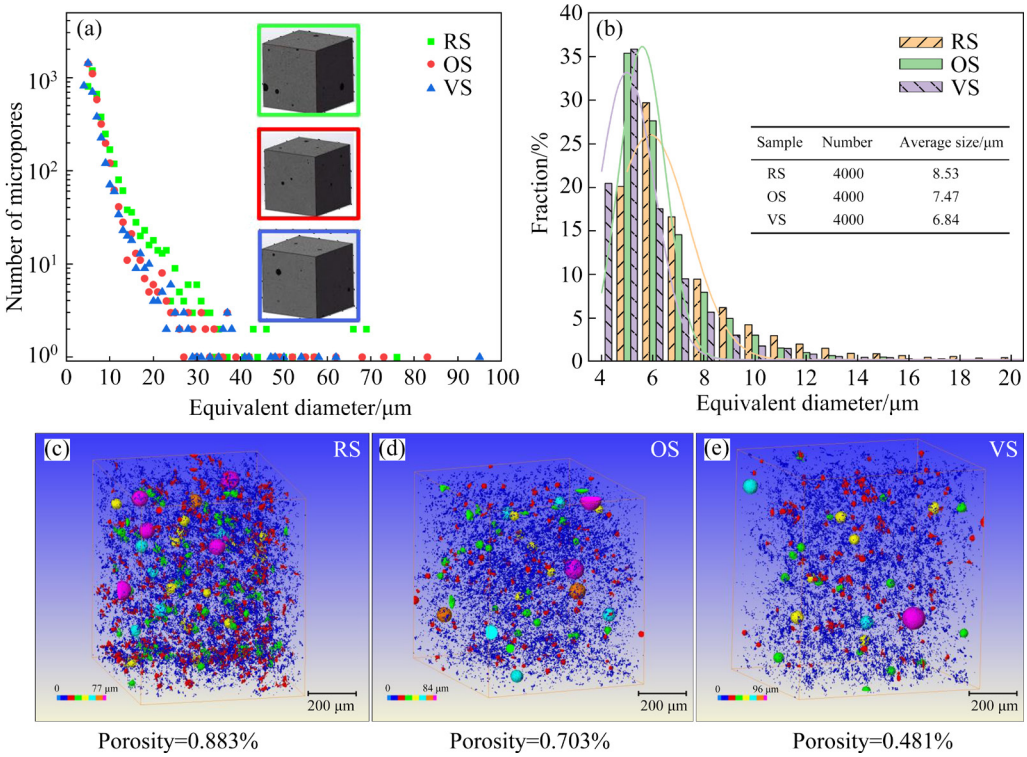

Fig. 5 Scattering diagram of equivalent diameter micropores (a); distribution diagram of micropores with RS, OS and VS strategies (b); 3D views of micropores with RS, OS and VS strategies (c−e)

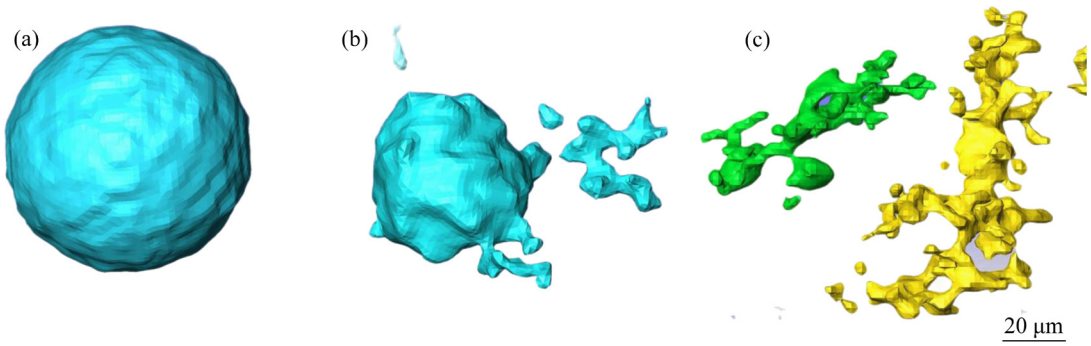

Fig. 6 Typical shapes of micropores: (a) Near-spherical micropore; (b) Rough surface micropore; (c) Chain-like micrpore

energetically favorable sites for the heterogeneous nucleation of hydrogen micropores during the solidification. The nucleated micropores grow with dendrite expansion, thereby appearing irregular in-wall structure. Lastly, the chain-like micropores have additional time to float, grow and combine with other micropores during deposition, as shown in Fig. 6(c). A considerable number of primary micropores that originally grow along dendrite arms aggregate into a chain or coarsen to larger ones [34]. Moreover, the bottom and middle regions experience additional heat cycles that act as a post-heat treatment for the previously deposited metals. Additional heat-induced secondary micropores and volume voids caused by dissolving eutectic phases are generated.

3.3 Microhardness

Figures 7(a−c) show the microhardness map of WAAM AA5356 components with three deposition strategies, and Figs. 7(d−f) show the microhardness distribution of these WAAM samples along deposition direction. The average microhardness values of WAAM AA5356 components with RS, OS, and VS strategies are HV 73.39, HV 75.52, and HV 76.16, respectively. The results indicate that the samples with OS and VS strategies have higher microhardness. The microhardness value along the deposition height fluctuates to different degrees under different deposition strategies. The microhardness values with RS strategy are stable, while those with OS and VS strategies fluctuate considerably. The microhardness values with OS and VS strategies show a downward trend along the deposition direction. In contrast, the microhardness values with OS strategy decrease in the top region, which is due to the aggregation of some micropores in the top region with OS strategy, as shown in Fig. 2(b) and Fig. 7(b).

Therefore, the microhardness distribution of these samples is further detected to analyze the difference. Overall, the microhardness of the components is uniform, which has a particular relationship with the uniformity of the microstructure. The microhardness also shows the stratification phenomenon. In the deposition state, the distribution of micropores is dispersed, and the second phase is relatively uniform, so the difference between microhardnesses is not very obvious. However, due to the high porosity with the RS strategy, the microhardness of the whole sample is low. The microhardness value of the sample is also related to the microstructure. With the increase in deposition height, the heat dissipation rate of the deposition layer slows down, and the grain grows.

Moreover, the grain size in the bottom region is significantly smaller than that in the top region, which leads to the downward trend of the microhardness value of the sample. The top region is open to the air and dissipates heat faster than the middle region. There are many micropores at the top of the preheating layer, which corresponds to the low microhardness value of the region. The highest microhardness value with VS strategy is due to the adjustment of the deposition path, resulting in the interactive thermal effect of components in the deposition process, thus leading to the formation of predominantly equiaxed grains and the minimal occurrence of porosity. According to the Hall−Petch relationship, the smaller the grain size, the greater the microhardness value. According to the data in Fig. 4 and Fig. 7, the RS

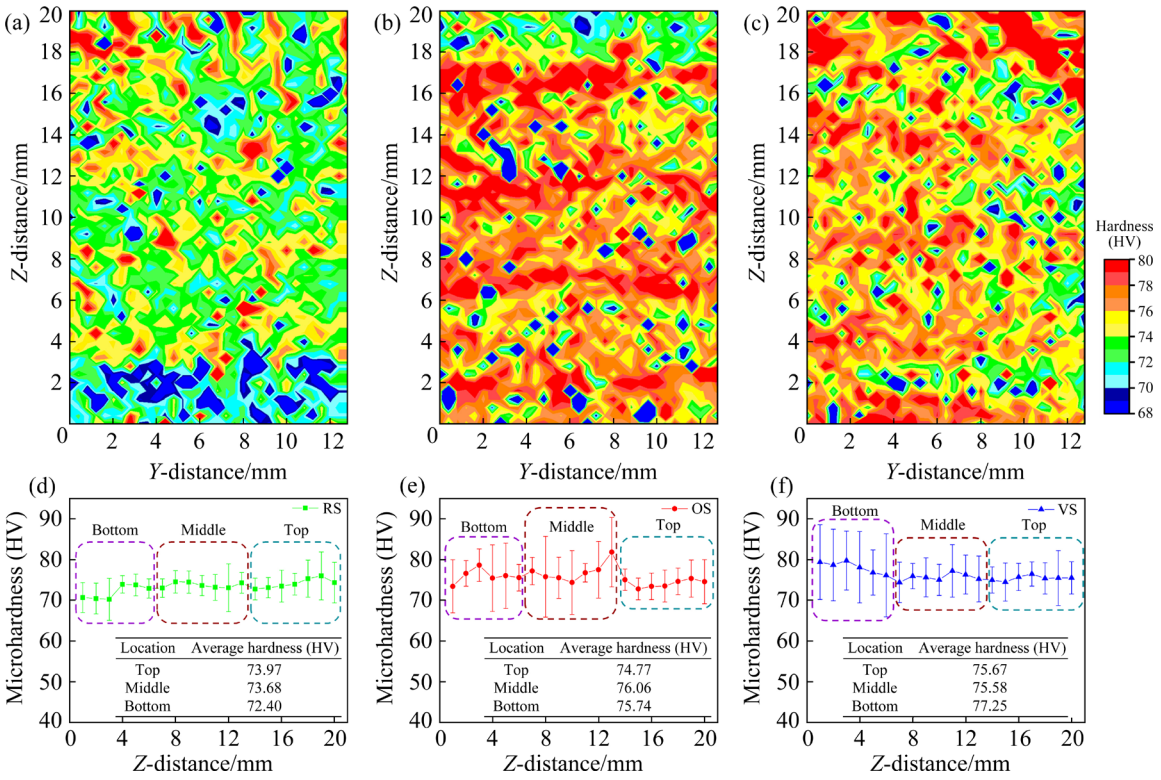

Fig. 7 Microhardness map and its distribution of WAAM AA5356 components: (a−c) Microhardness map with RS, OS and VS strategies, respectively; (d−f) Microhardness distribution with RS, OS and VS strategies, respectively

strategy has the smallest grain size, but its microhardness value is the lowest, in which the combined effect of fine grain strengthening and porosity defects on microhardness can be explained. The difference in grain diameter between the three deposition strategies is about 15 μm, which is not significant for a component with an original grain diameter of about 80 μm. While the porosity is reduced from 0.883% to 0.481%, the density of the component is significantly increased, and the microhardness is also improved.

3.4 Tensile properties

Figures 8(a−c) illustrate the ultimate tensile strength (UTS), yield strength (YS), and elongation results of WAAM AA5356 components with three deposition strategies in different tensile directions. There is no significant difference in the tensile results between the OS and VS strategies, and the tensile properties with RS strategy are the worst among the three deposition strategies. The UTS with OS and VS strategies are 28.39% and 34.32% higher than that with RS strategy, the YS with OS and VS strategies are 15.23% and 3.81% higher than that with RS strategy, and the elongations with OS and VS strategies are 41.27% and 40.21% higher than that with RS strategy, respectively. However, the tensile properties in the three directions are pretty different, which indicates that no matter the deposition strategy, the component has anisotropic tensile properties during the deformation.

For the same deposition strategy, the tensile performance of the sample in the *X*-direction is the best, and that of the sample in the *Y*-direction is the worst. As shown in Fig. 8(d), this is mainly because the tensile loading direction of the sample in the *Y*-direction is perpendicular to the molten pool interface, and there are aggregated micropores or even thermal cracks at the molten pool interface, which is the weakest position of the whole component [15]. It is well known that under uniaxial tensile loading, plastic deformation of metals preferentially occurs along slip planes oriented at 45° with respect to the loading direction, where shear stress reaches its maximum value [35]. The tensile strength is increased by a strengthening mechanism to stop the dislocation slip that leads to the plastic deformation. Therefore, the tensile performance of the sample in the *Y*-direction is the worst. For different deposition strategies, compared

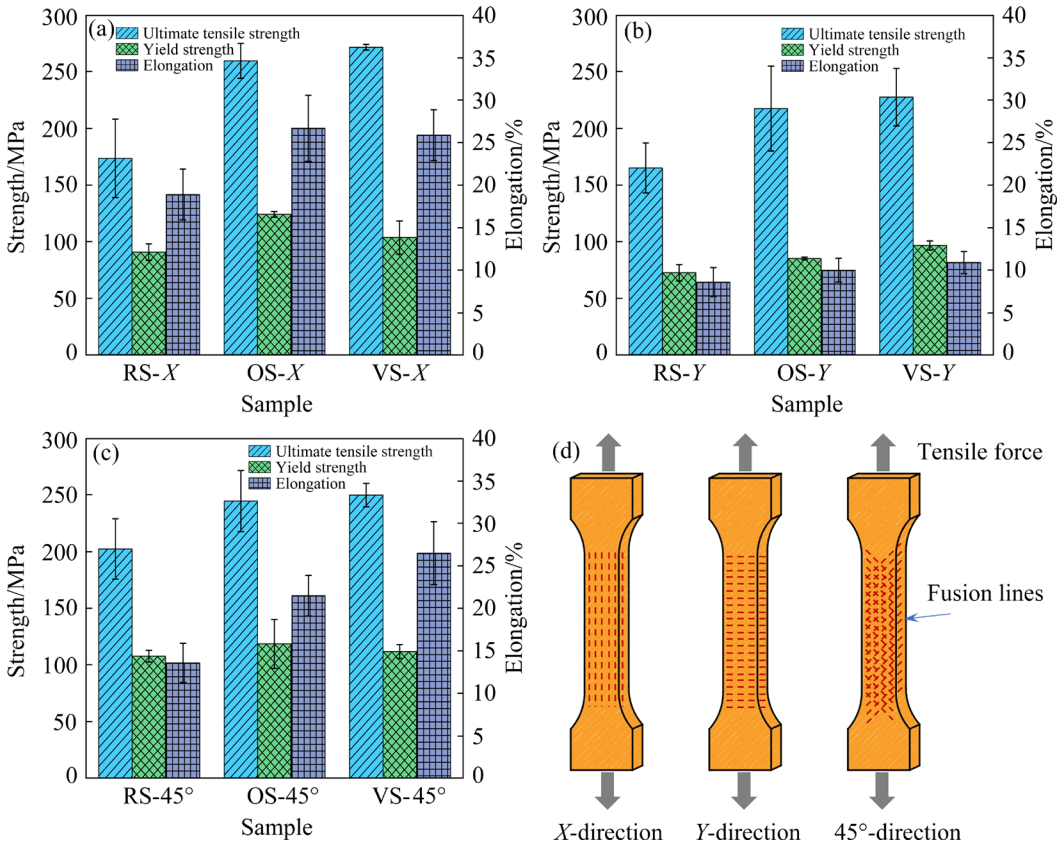

Fig. 8 Tensile properties of WAAM AA5356 components with RS, OS, and VS strategies in different tensile directions: (a) *X*-direction; (b) *Y*-direction; (c) 45°-direction; (d) Diagrams of different tensile directions

with OS and VS strategies, the tensile properties with RS strategy only reach the properties of ordinary cast 5356 aluminum alloy [36], which is mainly due to a large number of micropores in the components. At the same time, the grain size with RS strategy is the smallest among the three deposition strategies samples. For Al−Mg−Mn alloys, the larger the grain is, the longer the distance between grain boundaries is, the more freely the dislocation moves in the grain structure, and the better the ductility is [37]. Therefore, the tensile properties with RS strategy are the worst.

4 Conclusions

(1) The microstructures of the WAAM AA5356 components with three deposition strategies mainly consist of equiaxed and columnar grains. The grain sizes with OS and VS strategies are 21.82% and 8.26% larger than that with RS strategy, respectively. Higher heat inputs and slower cooling rates with OS and VS strategies result in coarser grain.

(2) The VS strategy effectively reduces the porosity from 0.883% to 0.481%, which is attributed to the melt pool overlap.

(3) The grain size increases while the microhardness decreases owing to the heat accumulation effect. The microhardnesses of the three deposition strategies samples are almost uniform. The minimum porosity and the smallest micropore are obtained with the VS strategy, leading to the best mechanical properties.

(4) The tensile properties with VS strategy in the *X*-direction are optimal, with an increase in UTS, YS and elongation of 34.32%, 3.81% and 40.21%, respectively, compared with those with RS strategy in the *X*-direction.

CRediT authorship contribution statement

Kai ZHU: Data curation, Writing − Original draft preparation; **Jian WANG:** Conceptualization, Methodology, Writing – Review & editing; **Wei-chen ZHANG:** Data curation, Visualization; **Xiao-lei ZHU:** Resources, Investigation; **Xiao-feng LU:** Supervision, Writing – Review & editing.

Declaration of competing interest

We declare that we have no financial and personal relationships with other people or organizations that can inappropriately influence our work. There is no professional or other personal interest of any nature or kind in any product, service and/or company that could be construed as influencing the position presented in, or the review of, the manuscript entitled.

Acknowledgments

This research was supported by the Postgraduate Research & Practice Innovation Program of Jiangsu Province, China (No. KYCX22_1311), the Natural Science Foundation of Jiangsu Province, China (No. BK20190684), and the Natural Science Research of the Jiangsu Higher Education Institutions of China (No. 18KJB460016).

References

[1] RODRIGUES T A, DUARTE V, MIRANDA R M, SANTOS T G, OLIVEIRA J P. Current status and perspectives on wire and arc additive manufacturing (WAAM) [J]. Materials (Basel), 2019, 12(7): 1121.

[2] WU Bin-tao, PAN Zeng-xi, DING Dong-hong, CUIURI D, LI Hui-jun, XU Jing, NORRISH J. A review of the wire arc additive manufacturing of metals: Properties, defects and quality improvement [J]. Journal of Manufacturing Processes, 2018, 35: 127−139.

[3] DEREKAR K S. A review of wire arc additive manufacturing and advances in wire arc additive manufacturing of aluminium [J]. Materials Science and Technology, 2018, 34: 895−916.

[4] NANDAN G, KUMAR G, ARORA K S, KUMAR A. MIG and CMT brazing of aluminum alloys and steel: A review [J]. Materials Today: Proceedings, 2022, 56: 481−488.

[5] SELVI S, VISHVAKSENAN A, RAJASEKAR E. Cold metal transfer (CMT) technology — An overview [J]. Defence Technology, 2018, 14: 28−44.

[6] TAWFIK M M, NEMAT-ALLA M M, DEWIDAR M M. Enhancing the properties of aluminum alloys fabricated using wire + arc additive manufacturing technique — A review [J]. Journal of Materials Research and Technology, 2021, 13: 754−768.

[7] WANG He, MA Shu-yuan, WANG Jia-chen, LU Tao, LIU Chang-meng. Microstructure and mechanical properties of TA15/TC11 graded structural material by wire arc additive manufacturing process [J]. Transactions of Nonferrous Metals Society of China, 2021, 31: 2323−2335.

[8] SAFARZADE A, SHARIFITABAR M, SHAFIEE A M. Effects of heat treatment on microstructure and mechanical properties of Inconel 625 alloy fabricated by wire arc additive manufacturing process [J]. Transactions of Nonferrous Metals Society of China, 2020, 30: 3016−3030.

[9] ALDALUR E, VEIGA F, SUÁREZ A, BILBAO J, LAMIKIZ A. High deposition wire arc additive manufacturing of mild steel: Strategies and heat input effect on microstructure and mechanical properties [J]. Journal of Manufacturing Processes, 2020, 58: 615−626.

[10] LUO Yi, LI Jing-long, XU Jie, ZHU Liang, HAN Jing-tao, ZHANG Cheng-yang. Influence of pulsed arc on the metal droplet deposited by projected transfer mode in wire-arc additive manufacturing [J]. Journal of Materials Processing and Technology, 2018, 259: 353−360.

[11] WAGIMAN A, BIN WAHAB M S, MOHID Z, MAMAT A. Effect of GMAW-CMT heat input on weld bead profile geometry for freeform fabrication of aluminium parts [J]. Applied Mechanics and Materials, 2013, 465/466: 1370−1374.

[12] SU Chuan-chu, CHEN Xi-zhang, GAO Chuang, WANG Yang-fan. Effect of heat input on microstructure and mechanical properties of Al−Mg alloys fabricated by WAAM [J]. Applied Surface Science, 2019, 486: 431−440.

[13] BAI J Y, FAN C L, LIN S B, YANG C L, DONG B L. Effects of thermal cycles on microstructure evolution of 2219-Al during GTA-additive manufacturing [J]. The International Journal of Advanced Manufacturing Technology, 2016, 87: 2615−2623.

[14] XIONG Jun, LEI Yang-yang, CHEN Hui, ZHANG Guang-jun. Fabrication of inclined thin-walled parts in multi-layer single-pass GMAW-based additive manufacturing with flat position deposition [J]. Journal of Materials Processing and Technology, 2017, 240: 397−403.

[15] DEREKAR K, LAWRENCE J, MELTON G, ADDISON A, ZHANG Xiang, XU Lei. Influence of interpass temperature on wire arc additive manufacturing (WAAM) of aluminium alloy components [J]. MATEC Web of Conferences, 2019, 269: 05001.

[16] JAFARI D, VANEKER T H J, GIBSON I. Wire and arc additive manufacturing: Opportunities and challenges to control the quality and accuracy of manufactured parts [J]. Materials & Design, 2021, 202: 109471.

[17] OYAMA K, DIPLAS S, M'HAMDI M, GUNNÆS A E, AZAR A S. Heat source management in wire-arc additive manufacturing process for Al−Mg and Al−Si alloys [J]. Additive Manufacturing, 2019, 26: 180−192.

[18] GU Jiang-long, DING Jia-luo, WILLIAMS S W, GU Hui-min, BAI Jing, ZHAI Yu-chun, MA Pei-hua. The strengthening effect of inter-layer cold working and post-deposition heat treatment on the additively manufactured Al−6.3Cu alloy [J]. Materials Science and Engineering A, 2016, 651: 18−26.

[19] MIAO Qiu-yu, WU Dong-jiang, CHAI Dong-sheng, ZHAN Yu, BI Gui-jun, NIU Fang-yong, MA Guang-yi. Comparative study of microstructure evaluation and mechanical properties of 4043 aluminum alloy fabricated by wire-based additive manufacturing [J]. Materials & Design, 2020, 186: 108205.

[20] KLEIN T, ARNOLDT A, LAHNSTEINER R, SCHNALL M. Microstructure and mechanical properties of a structurally refined Al−Mg−Si alloy for wire-arc additive manufacturing [J]. Materials Science and Engineering A, 2022, 830: 142318.

[21] CABALLERO A, DING Jia-luo, GANGULY S, WILLIAMS S. Wire + arc additive manufacture of 17-4 PH stainless steel: Effect of different processing conditions on microstructure, hardness, and tensile strength [J]. Journal of

Materials Processing and Technology, 2019, 268: 54−62.
[22] SYED A K, ZHANG Xiang, CABALLERO A, SHAMIR M, WILLIAMS S. Influence of deposition strategies on tensile and fatigue properties in a wire + arc additive manufactured Ti−6Al−4V [J]. International Journal of Fatigue, 2021, 149: 106268.
[23] XU Xiang-fang, DING Jia-luo, GANGULY S, DIAO Cheng-lei, WILLIAMS S. Preliminary investigation of building strategies of maraging steel bulk material using wire + arc additive manufacture [J]. Journal of Materials Engineering and Performance, 2019, 28: 594−600.
[24] MA Guo-cai, ZHAO Gang, LI Zhi-hao, YANG Min, XIAO Wen-lei. Optimization strategies for robotic additive and subtractive manufacturing of large and high thin-walled aluminum structures [J]. The International Journal of Advanced Manufacturing Technology, 2019, 101: 1275−1292.
[25] LEE S G, GOKHALE A M. Formation of gas induced shrinkage porosity in Mg-alloy high-pressure die-castings [J]. Scripta Materialia, 2006, 55: 387−390.
[26] CONG Bao-qiang, DING Jia-luo, WILLIAMS S. Effect of arc mode in cold metal transfer process on porosity of additively manufactured Al−6.3%Cu alloy [J]. The International Journal of Advanced Manufacturing Technology, 2015, 76: 1593−1606.
[27] ZHANG Chen, GAO Ming, ZENG Xiao-yan. Workpiece vibration augmented wire arc additive manufacturing of high strength aluminum alloy [J]. Journal of Materials Processing and Technology, 2019, 271: 85−92.
[28] WANG Jian, ZHU Kai, ZHANG Wei-chen, ZHU Xiao-lei, LU Xiao-feng. Microstructural and defect evolution during WAAM resulting in mechanical property differences for AA5356 component [J]. Journal of Materials Research and Technology, 2023, 22: 982−996.
[29] LI Geng, ZHANG Chen, GAO Ming, ZENG Xiao-yan. Role of arc mode in laser-metal active gas arc hybrid welding of mild steel [J]. Materials & Design, 2014, 61: 239−250.
[30] WANG Fu-de, WILLIAMS S, RUSH M. Morphology investigation on direct current pulsed gas tungsten arc welded additive layer manufactured Ti_6Al_4V alloy [J]. The International Journal of Advanced Manufacturing Technology, 2011, 57: 597−603.
[31] ZHANG Chen, LI Yu-fei, GAO Ming, ZENG Xiao-yan. Wire arc additive manufacturing of Al−6Mg alloy using variable polarity cold metal transfer arc as power source [J]. Materials Science and Engineering A, 2018, 711: 415−423.
[32] BOEIRA A P, FERREIRA I L, GARCIA A. Alloy composition and metal/mold heat transfer efficiency affecting inverse segregation and porosity of as-cast Al−Cu alloys [J]. Materials & Design, 2009, 30: 2090−2098.
[33] WANG Qing-tao, WANG Xiao-nan, CHEN Xia-ming, HUAN Peng-cheng, DONG Qi-peng, ZHANG Qing-yu, NAGAUMI H. Interactive effects of porosity and microstructure on strength of 6063 aluminum alloy CMT MIX + synchropulse welded joint [J]. Transactions of Nonferrous Metals Society of China, 2022, 32: 801−811.
[34] GU Jiang-long, GAO Min-jie, YANG Shuo-liang, BAI Jing, DING Jia-luo, FANG Xue-wei. Pore formation and evolution in wire + arc additively manufactured 2319 Al alloy [J]. Additive Manufacturing, 2019, 30: 100900.
[35] LAGHI V, PALERMO M, TONELLI L, GASPARINI G, CESCHINI L, TROMBETTI T. Tensile properties and microstructural features of 304L austenitic stainless steel produced by wire-and-arc additive manufacturing [J]. The International Journal of Advanced Manufacturing Technology, 2020, 106: 3693−3705.
[36] WANG Jian-kun, SHEN Qing-kai, KONG Xiang-dong, CHEN Xi-zhang. Arc additively manufactured 5356 aluminum alloy with cable-type welding wire: Microstructure and mechanical properties [J]. Journal of Materials Engineering and Performance, 2021, 30: 7472−7478.
[37] PANCHENKO O, KURUSHKIN D, MUSHNIKOV I, KHISMATULLIN A, POPOVICH A. A high-performance WAAM process for Al−Mg−Mn using controlled short-circuiting metal transfer at increased wire feed rate and increased travel speed [J]. Materials & Design, 2020, 195: 109040.

沉积策略对电弧增材制造 5356 铝合金显微组织、缺陷和力学性能的影响

朱 凯，王 健，张炜辰，朱晓磊，陆晓峰

南京工业大学 机械与动力工程学院，南京 211816

摘 要：基于电弧增材制造技术(WAAM)研究往复扫描(RS)、振荡扫描(OS)和垂直扫描(VS) 3 种沉积策略对 5356 铝合金(AA5356)构件的影响，探讨 5356 铝合金构件的显微组织、缺陷和力学性能。结果表明：相比于 RS 和 OS 策略，VS 策略使得构件的热量分布均匀。VS 策略的显微组织主要由等轴晶组成，使得显微硬度最高值达到 HV 77.25。VS 策略使得构件的气孔率和微孔尺寸分别下降了 45.52%和 19.81%，从而改善了拉伸性能。因此，VS 策略为获得显微组织均匀、力学性能优异的 AA5356 构件提供了一种新的解决方案。

关键词：电弧增材制造；沉积策略；铝合金；显微组织；力学性能

(Edited by Wei-ping CHEN)